Investigation of Electrochemical Transport, Gate Leakage, and Transconductance Behavior in PEDOT:PSS Organic Electrochemical Transistors

Vinay Budhraja[z 1], Bilal Khan[1], Abijeet Singh Mehta[2]
[1]Department of Electrical Engineering, Northern Illinois University, DeKalb IL, USA
[2]Department of Health and Biomedical Sciences, University of Texas Rio Grande Valley, TX, USA
[z]vbudhraja@niu.edu

Abstract

Organic Electrochemical Transistors (OECTs) are promising candidates for low-voltage bioelectronic systems due to their high transconductance, mixed ionic–electronic transport, and compatibility with flexible substrates. In this work, we investigate the electrochemical transport, gate leakage, and transconductance behavior of screen-printed PEDOT:PSS OECTs, with emphasis on the relationship between ionic coupling and output characteristics. Key electrical and electrochemical parameters—including drain current modulation, transconductance evolution, gate current behavior, and capacitance–voltage response—were systematically analyzed to elucidate the mechanisms governing device operation. The results reveal clear trade-offs between parasitic resistance, volumetric electrochemical capacitance, and effective gate control, which in turn influence signal integrity and amplification efficiency. Devices exhibiting reduced parasitic effects demonstrated lower gate leakage, improved signal-to-noise ratio, and more stable transconductance, whereas devices with stronger ionic coupling showed enhanced drain current at the expense of nonlinearity in the saturation regime. High-frequency C–V measurements and gate-current modeling further confirm distinct electrochemical dynamics driven by modulation of mixed conduction pathways. These insights provide a deeper understanding of OECT operation and offer practical guidelines for optimizing device architectures in solid-state and flexible bioelectronic applications.

Introduction

Organic Electrochemical Transistors (OECTs) were first introduced in 1984 by White, Kittlesen, and Wrighton, who demonstrated a device capable of modulating conductivity through electrochemical doping of a conducting polymer[1]. Since then, OECTs have emerged as a transformative class of devices in bioelectronics, offering a unique platform for converting biochemical and ionic signals into amplified electronic responses[2-4]. Their operating mechanism is based on electrochemical modulation of channel conductivity via ion exchange between the gate electrode and the conducting polymer through an electrolyte[5,6]. This mechanism, enabled by ionic penetration from an electrolyte into a conducting polymer such as PEDOT:PSS, results in high transconductance, low-voltage operation, and stable performance in aqueous and dynamic environments[7-9].

These attributes have positioned OECTs as promising candidates for wearable, implantable, and flexible sensing platforms, including applications in neurotransmitter monitoring, metabolite detection, on-skin diagnostics, and tissue-interface measurements[10-14]. In these systems, OECTs act as local signal amplifiers capable of interfacing directly with biological environments, eliminating the need for traditional solid-state gate dielectrics and enabling safe operation below 1 V. The compatibility of OECTs with mechanically compliant substrates and

processing routes further supports their integration into emerging soft-electronics technologies and distributed biosensor networks. As research has advanced, theoretical and experimental studies have highlighted the critical role of electrochemical capacitance, polymer morphology, and device geometry in governing OECT performance metrics such as drain current modulation, and transient response [15]. Experimental studies have further shown that polymer morphology, electrolyte composition, and device geometry strongly affect figures of merit including drain current, transconductance, response speed, and operational stability[16–18]. At the same time, parasitic resistances, interfacial polarization, and gate leakage introduce non-idealities that distort transistor response, reduce signal-to-noise ratio, and limit long-term sensing fidelity. Unlike MOSFETs, where the gate stack prevents DC pathways, OECTs allow ionic exchange at the gate interface, making leakage currents an intrinsic part of device operation. Understanding this behavior is particularly important for low-power and continuous biosensing applications, where even small leakage pathways can degrade baseline stability.

Recent advances in additive manufacturing have accelerated interest in printed OECTs, which offer low-cost, scalable fabrication on flexible substrates without the need for cleanroom processing[19–24]. However, printed OECTs often exhibit more pronounced parasitic effects, non-uniform ionic coupling, and greater performance variability compared to microlithographic counterparts. While numerous studies have focused on sensing demonstrations or material innovations, fewer works have systematically examined how electrochemical transport, transconductance evolution, and leakage behavior interact to define the baseline performance of printed devices. This gap has limited the development of predictive design rules for stable, low-power OECT operation in large-area and flexible systems.

In this work, we investigate the electrochemical transport, gate leakage, and transconductance behavior of screen-printed OECTs. Through electrical characterization, capacitance measurements, and gate-current analysis, we elucidate the mechanisms governing device performance and identify the trade-offs that arise from electrochemical coupling and parasitic pathways. The insights provided here contribute to the fundamental understanding of printed OECT operation and offer practical guidelines for improving device stability, minimizing leakage effects, and optimizing transconductance in low-power solid-state and bioelectronic applications.

Experimental

Flexible Organic Electrochemical Transistors (OECTs) were fabricated on polyethylene terephthalate (PET) substrates. Prior to printing, PET sheets were cleaned with isopropyl alcohol (IPA) and deionized (DI) water, followed by drying under nitrogen flow at room temperature. Source, drain, and gate electrodes were patterned using a stainless-steel screen and an AMI MSP-485 screen printer. A commercial silver (Ag) conductive ink was deposited and cured at 120 °C for 5 minutes to ensure adequate adhesion and conductivity. The channel width (W) was defined in the printed layout, and all electrodes were patterned in a single print step to ensure alignment. The OECT channel was printed using PEDOT:PSS solution directly over the source and drain electrodes. The film was annealed at 50 °C for 5 minutes to achieve a uniform, conductive polymer layer that electrically connected the source and drain electrodes. An insulating layer of polymethyl methacrylate (PMMA) was then applied to cover the metal contacts, protecting source and drain electrodes from electrolyte exposure. For ionic gating, 5

µL of sodium polystyrene sulfonate (PSSNa) electrolyte was deposited through a shadow mask onto the PEDOT:PSS channel. The device was then cured at 60 °C for 10 minutes to ensure slow solvent evaporation and form a stable ionic layer.

The complete OECT device architecture, including electrode geometry and channel layout, is shown in Fig. 1a, while a top-view image of the final device is presented in Fig. 1b. For each geometry, a batch of six devices (n = 6) was fabricated and tested to ensure statistical reliability of the results. The structural quality of the printed layers and the Ag–PEDOT:PSS interface was examined via Scanning Electron Microscopy (SEM). Energy dispersive X-ray spectroscopy (EDS) reports the presence of around 15% sulfur which validates the presence of PEDOT in the PEDOT: PSS[25]. The optical thickness and homogeneity of the PEDOT:PSS film were analyzed using a Filmetrics F40-UV thin-film analyzer. Electrical characterization was conducted using a Keithley 4200-SCS Parametric Analyzer. The output and transfer characteristics of the OECTs were measured to extract transconductance, threshold voltage, and ON/OFF current ratios. Capacitance–voltage (C–V) measurements were performed to study the electrochemical gating behavior. In addition, gate leakage currents and parasitic resistances were analyzed using circuit models adapted from Friedlein et al.[21], enabling a deeper understanding of device performance and non-idealities.

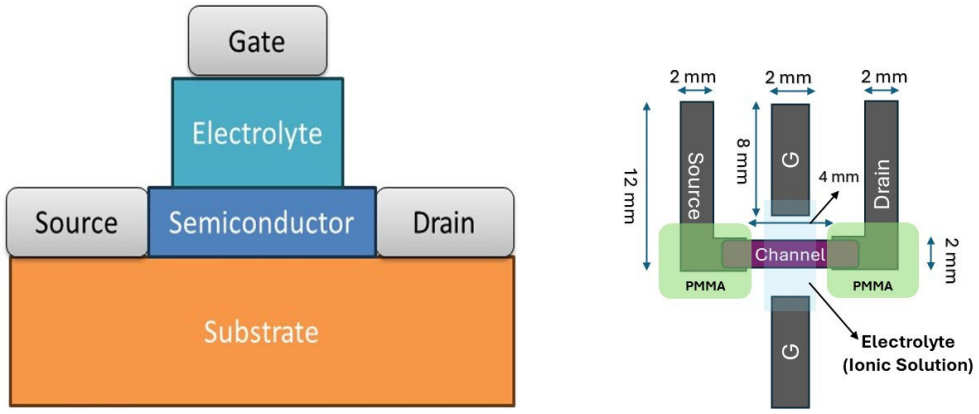

(a) **(b)**

Figure 1 (a) Schematic cross-sectional view of the fabricated Organic Electrochemical Transistor (OECT), illustrating the printed silver source, drain, and gate electrodes, the PEDOT:PSS channel, insulating PMMA layer, and the PSSNa electrolyte. (b) Top-view optical image of the fabricated OECT structure showing the screen-printed silver electrodes and the drop-cast PEDOT:PSS channel.

Figure 2(a) displays the schematic illustration of the printed OECT. The high-magnification surface images of thin films were obtained by scanning electron microscopy (SEM, Jeol, Inc., USA). Energy dispersive Xray spectroscopy (EDS) at a landing voltage of 10.0 kV reports the presence of 18.1±0.21% of sulfur which validates the presence of PEDOT in the PEDOT: PSS composite (Figure 2b). As PEDOT is a conducting polymer composed of repeating units of

ethylenedioxythiophene, the presence of sulfur confirms the thiophene moiety in the PEDOT backbone. SEM images of silver, PEDOT: PSS and the interface of silver versus PEDOT: PSS are shown in figures 2 c, 2d and 2e respectively.

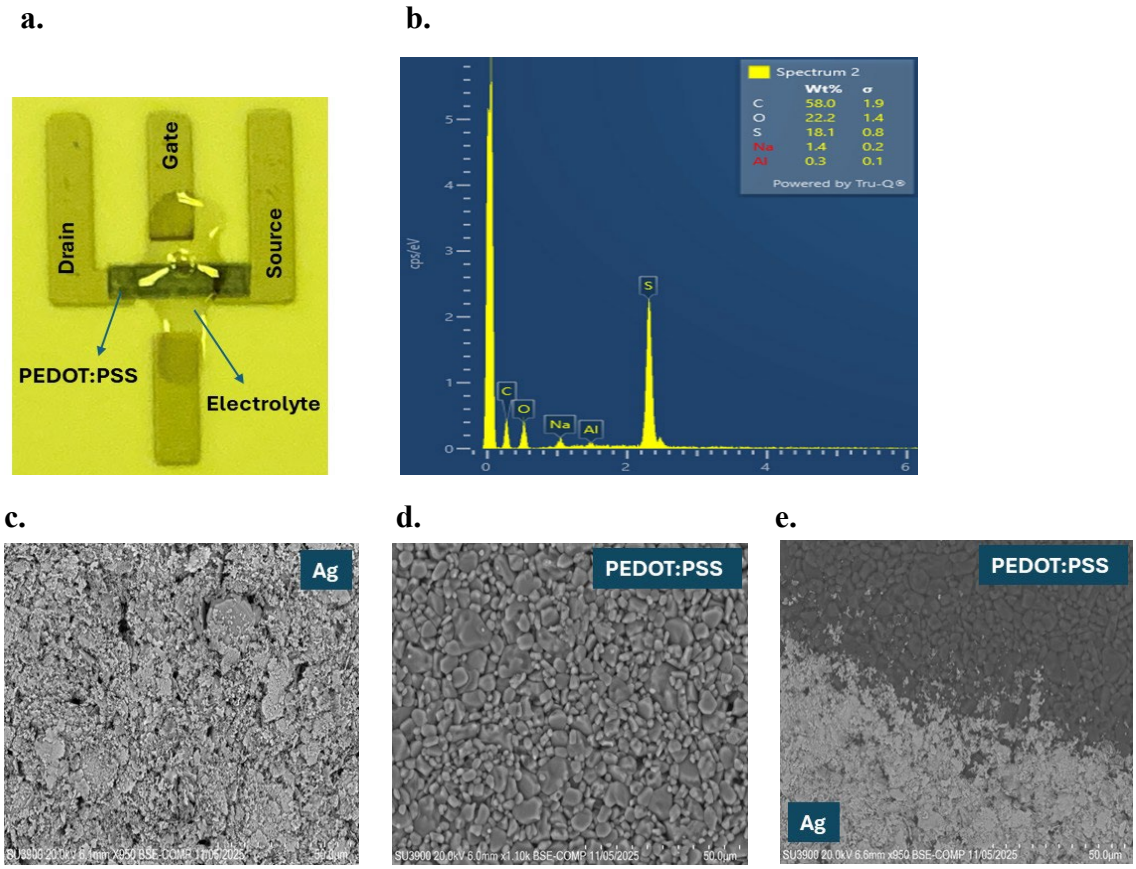

Figure 2. (a) Schematic illustration of the OECT. **(b)** EDS results of the semiconducting channel, where the inset shows the % of the presence of Sulfur. SEM images of **(c)** Ag film, **(d)** PEDOT: PSS channel **(e)** Ag-PEDOT: PSS interface at a 50 µm magnification.

Results and Discussion

The printed OECTs exhibited depletion-mode operation, where the application of a positive gate bias reduced the drain current through electrochemical dedoping of the PEDOT:PSS channel. The output characteristics (Figure 3a) show the expected transition from the linear to saturation regime, confirming effective electrochemical gating of the channel. The corresponding transfer curves (Figure 3b) further validate stable modulation of channel conductivity over the applied voltage range, characteristic of depletion-mode PEDOT:PSS OECTs. As the gate potential increased, cation injection from the electrolyte compensated the negatively charged sulfonate groups in PEDOT:PSS, driving the material toward a less conductive, dedoped state and resulting in the observed current reduction.

The channel resistance (R_{ch}) is given by:

$$R_{ch}\ \alpha\ \frac{L}{W.\sigma} \qquad (1)$$

where L is the channel length, W is the channel width, and σ is the electrical conductivity of the channel.

The observed I–V response aligns with the mixed ionic–electronic transport characteristics of PEDOT:PSS, where electrochemical doping occurs volumetrically rather than at a narrow interfacial region, as seen in traditional OFETs. The transfer characteristics (Figure 3 b) confirm depletion-mode operation, in which increasingly positive gate voltages reduce channel conductivity through electrochemical de-doping of PEDOT: PSS.

The transconductance (g_m), a key figure of merit for amplification and sensing applications, was extracted from the slope of the transfer curve in the linear region using:

$$g_m = \frac{\partial I_D}{\partial V_G} \tag{2}$$

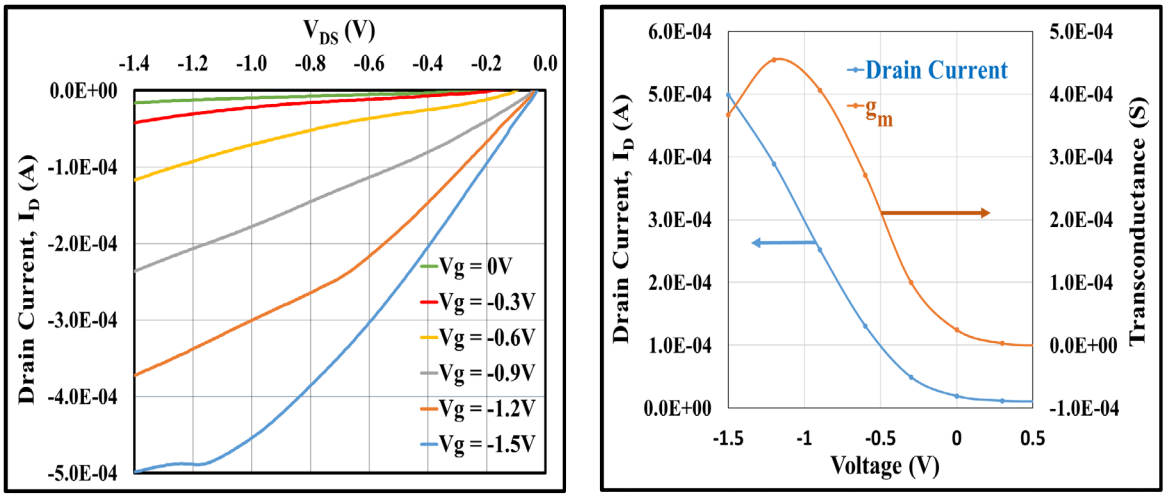

(a) (b)

Figure 3. (a) Output characteristics (I_D vs. V_{DS}) of OECTs; **(b)** Transfer characteristics (I_D vs. V_{GS}) at V_{DS} = –0.6 V showing depletion-mode behavior and extracted transconductance.

The extracted g_m characteristics are presented in Figure 4. The devices exhibited well-defined transconductance peaks, indicative of effective volumetric modulation of the channel. Normalized g_m analysis suggests that volumetric capacitance, ionic accessibility, and parasitic resistances collectively govern the amplification behavior and the position of the g_m maximum. These trends are consistent with mixed-transport OECT models, where the spatial distribution of dopants and the voltage drop at the electrolyte/channel interface play a dominant role in defining device response.

The transconductance of the OECTs was extracted from the slope of the transfer curves using the expression:

$$g_m = \begin{cases} -\mu C^* \frac{Wd}{L} V_D, & for\ V_D > V_G - V_T \\ -\mu C^* \frac{Wd}{L} [V_G - V_T], & for\ V_D < V_G - V_T \end{cases} \tag{3}$$

where μ is the hole mobility, g_m is the transconductance, C* is the volumetric capacitance,

W, d, L are the channel width, thickness and length respectively.

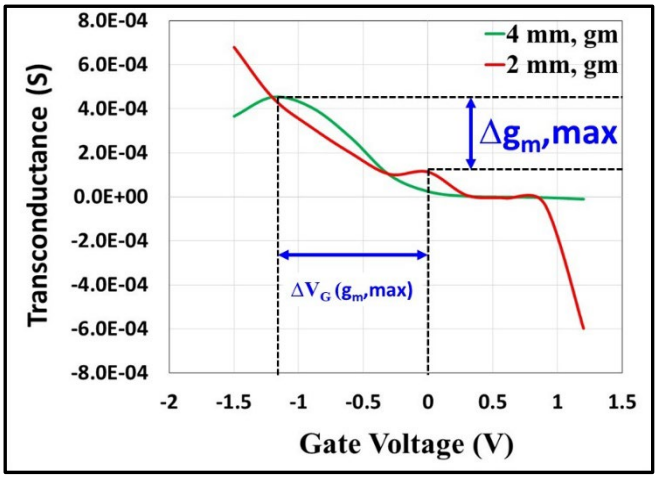

Figure 4. Extracted transconductance (g_m) as a function of gate voltage (V_{GS}) for OECTs with 2 mm and 4 mm channel lengths.

Parasitic resistance arises from the interfaces between the PEDOT:PSS channel and the metallic electrodes, and acts as a series element between the active channel and the external circuit[6, 21, 26]. This series resistance modifies the effective gate voltage seen by the channel, resulting in- the shift of the g_m peak to more positive V_{GS}, suppression of peak transconductance, increased signal distortion, and reduced unity-gain frequency in amplifier configurations.

Deviations from ideal behavior can be attributed to parasitic resistances—primarily contact and electrolyte–channel interfacial resistance—which alter the effective gate potential experienced by the channel. As previously reported by Friedlein *et al.*[27], parasitic elements suppress the peak transconductance, distort the transfer response, and limit high-frequency performance, trends that are also reflected in our devices.

Overall, the electrical response confirms efficient electrochemical gating, stable depletion-mode operation, and reproducible transconductance behavior, demonstrating the suitability of the printed PEDOT:PSS OECTs for sensing and amplification applications.

Gate leakage behavior is a defining distinction between Organic Electrochemical Transistors (OECTs) and conventional Metal–Oxide–Semiconductor Field-Effect Transistors (MOSFETs). In MOSFETs, the gate is separated from the semiconductor by a solid dielectric (e.g., SiO_2), which suppresses charge transfer and leads to gate currents on the order of picoamperes. OECTs, however, employ an electrolyte as the gate insulator. The presence of mobile ions in the electrolyte lowers the effective resistance between the gate and channel, creating a possible faradaic or ionic pathway for measurable gate current (I_G). Figure 5 highlights these differences, illustrating the device stacks and corresponding energy level diagrams of MOSFET and OECT structures. The Fermi level in the electrolyte $(E_{F,E})$shifts with ion accumulation at the interface, modifying the effective gate capacitance and enabling direct electrochemical modulation of the channel [27, 28].

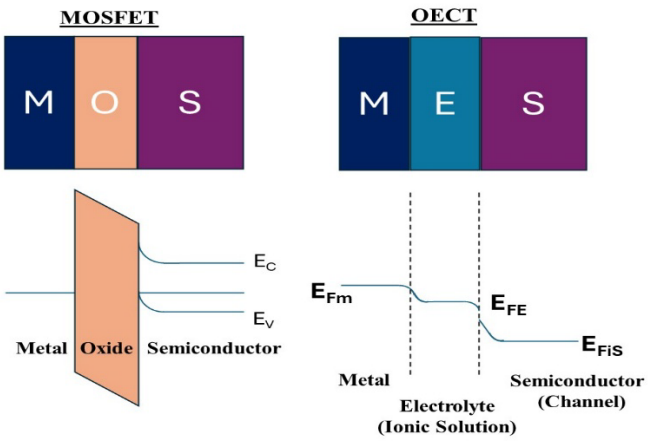

Figure 5. Energy band diagram comparison between MOSFET and OECT. Device architecture illustrating the different gate interfaces: a solid dielectric (oxide) in MOSFET and an ion-conducting electrolyte in OECT.

While traditional MOSFET models assume $I_G \approx 0$, such assumptions are not always valid for OECTs. Several modeling studies[21, 27, 29, 30] idealize the gate–electrolyte–channel interface and neglect leakage contributions. However, in practical OECTs, I_G can provide valuable information, especially in sensing scenarios where redox activity or interfacial charge-transfer processes occur. Therefore, evaluating gate current is essential for understanding electrochemical isolation, stability, and signal fidelity.

Figure 6 a shows the measured I_G versus V_{DS} for the printed OECTs. Short-channel devices exhibited low leakage, with I_G in the range of 10^{-7} to 10^{-6} A across the applied bias window, indicating strong electrochemical isolation between gate and channel. In contrast, longer-channel devices showed higher gate leakage, reaching approximately -3.5×10^{-5} A at $V_{DS} = -1.5$ V. A similar trend was observed in the I_G–V_{GS} sweeps (Figure 6 b), suggesting that electrolyte path length and interfacial area influence leakage behavior.

The gate-dependent transconductance response was evaluated using:

$$g_{ds} = \frac{\partial I_D}{\partial V_G} \tag{4}$$

For short-channel OECTs, the negligible I_G enables simplified models where electrochemical gating can be approximated using MOSFET-like assumptions. This observation is consistent with the findings of Zabihipour *et. al.*[31], where devices with reduced channel dimensions exhibited leakage currents insignificant relative to the drain current. In contrast, non-negligible I_G in longer channels introduces parasitic electrochemical pathways that affect both DC and transient response.

The impact of leakage was further evaluated through signal-to-noise ratio (SNR) analysis and current stability. Devices exhibiting higher I_G showed 5–8% fluctuation in drain current under repeated operation, reducing SNR from ~32 to ~18 and indicating increased electrochemical noise. Additionally, elevated leakage represents excess power consumption, which is undesirable for wearable or battery-powered sensing systems. These results demonstrate that minimizing I_G is not only critical for accurate modeling, but also for improving sensing resolution, stability, and energy efficiency in OECT-based platforms.

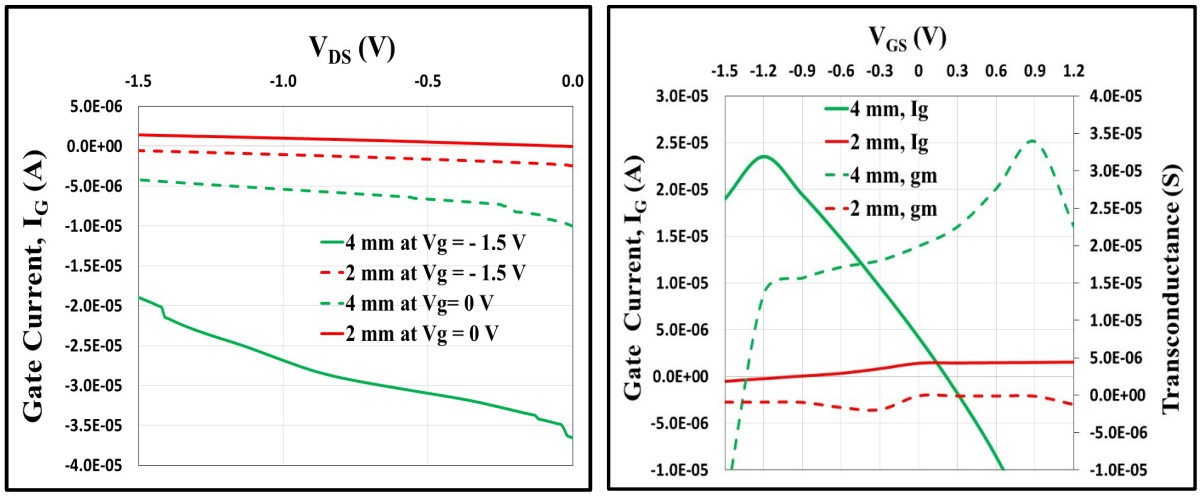

(a) (b)

Figure 6. Gate leakage current analysis in OECTs with different channel lengths. **(a)** I_G vs. V_{DS} characteristics at V_G= 0 V and 1.5 V for 2 mm and 4 mm channel devices; **(b)** I_G and transconductance (g_{ds}) as a function of V_{GS} for the same devices.

To gain a deeper understanding of the role of gate current in device operation, numerical modeling of the OECT structure was performed in MATLAB. The equations used in this study were adapted from the frameworks developed by Skowronski *et. al.*[32] and Shirinskaya *et. al.*[33]. Unlike MOSFETs, where the displacement current at the gate terminal vanishes once the dielectric is fully charged, OECTs exhibit finite gate current due to ionic transport through the electrolyte. In these devices, ions balance electronic charge in the channel, and although the source and drain electrodes block ionic flow, the gate terminal remains an active electrochemical interface.

The total gate current, I_G, arises from two dominant mechanisms: (i) ionic displacement within the electrical double layer, and (ii) electrochemical reactions at the gate/electrolyte or channel/electrolyte interface. Depending on the gate electrode material, two characteristic gating behaviors are observed[14]: (1) Polarizable gates (e.g., Ag/AgCl, Pt): behave as ideal capacitors with negligible faradaic charge transfer; (2) Non-polarizable gates (e.g., PEDOT:PSS, carbon): allow redox processes, modeled as a capacitor in parallel with a resistor. In both cases, the gate current is non-zero and must be included in transient OECT models. The total current is expressed as:

$$I_G(t) = I_{\text{cap}}(t) + I_{\text{faradaic}}(t) \qquad (5)$$

where the capacitive and faradaic components are given by:

$$I_{\text{cap}}(t) = C_{\text{dl}} \frac{\partial V_G(t)}{\partial t} \qquad (6)$$

$$I_{\text{faradaic}}(t) = C_{\text{dl}} \frac{V_G(t) - V_{\text{redox}}}{R_f} \qquad (7)$$

Here, $C_{\text{dl}}$is the double-layer capacitance, $R_f$is the faradaic resistance, and $V_{\text{redox}}$is the redox

potential of the gate–electrolyte interface.

Because the channel current responds to both electrochemical modulation and gate-induced ionic motion, the transient drain current can be expressed as[34]:

$$I_D(t) = I_0 - f\, I_G(t) + \Delta I_{ch} = I_0 - f\, I_G(t) \mp g_m V_{ch}(t) \quad (8)$$

where I_0 is the steady-state drain current, f is the fraction of gate current that redistributes to source or drain, and $V_{\mathrm{ch}}(t)$ is the time-dependent channel potential.

MATLAB simulations were performed to model gate current in OECTs under different gate configurations. For the polarizable gate, the system was modeled as a pure capacitor with a Gaussian voltage pulse input, and gate current was calculated as $I_G = I_{cap}$. For the non-polarizable gate, a sinusoidal gate voltage was applied to a parallel RC circuit, and the total gate current was computed using $I_G = I_{cap} + I_{faradaic}$. These models capture the dominant capacitive transient in polarizable gates and the persistent faradaic contribution in non-polarizable electrodes.

Figure 7 illustrates the gate current components in an OECT with a polarizable gate electrode, where gate voltage $V_G(t)$ modeled as a Gaussian pulse to simulate a transient event. The total current is dominated by a sharp transient capacitive peak, consistent with ideal double-layer charging behavior and negligible faradaic contribution.

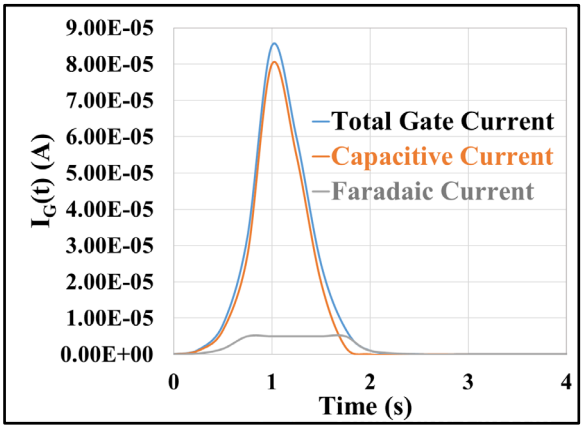

Figure 7. Simulated gate current in an OECT with a polarizable gate electrode. The gate voltage was modeled as a Gaussian pulse to simulate a transient input

For non-polarizable gates, a sinusoidal input was applied to a parallel RC model, yielding a combination of capacitive and persistent faradaic contributions. As shown in Figure 8, the sinusoidal forcing produces a phase-shifted capacitive current superimposed on a sustained faradaic component, demonstrating that I_G remains non-zero throughout the cycle.

Importantly, these results emphasize that unlike traditional MOSFETs—where the gate current is typically negligible—the gate current in OECTs plays an active role in the device's electrochemical dynamics. It must be considered when analyzing device stability, sensing response, or signal integrity in bioelectronic applications. Neglecting this current may result in an incomplete understanding of device behavior, particularly in systems employing non-polarizable or functionalized gate materials.

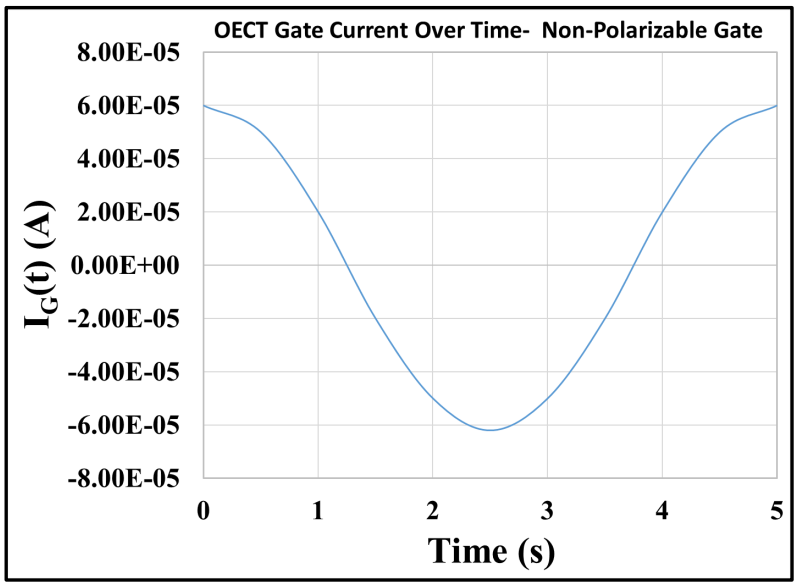

Figure 8. Simulated gate current in an OECT with a non-polarizable gate electrode under sinusoidal gate bias.

Overall, minimizing gate leakage contributes to improved energy efficiency, reduced noise, and enhanced device stability. This makes OECTs particularly attractive for low-power, noise-resilient bioelectronic applications. The comparison with MOSFETs underscores the unique electrochemical nature of OECTs and highlights the need for tailored models that accurately represent their mixed ionic-electronic transport behavior. Therefore, accurate OECT compact models must incorporate ionic motion and interfacial charge-transfer processes rather than assuming an ideal insulating gate.

Organic Electrochemical Transistors (OECTs) are widely investigated for biosensing and impedance-based diagnostics; however, the interplay between device geometry, interfacial capacitance, and operating frequency remains not fully resolved. To clarify these effects, we analyze the capacitive behavior of printed OECTs with different channel lengths under high-frequency C–V excitation, with the goal of isolating intrinsic device properties from electrode–electrolyte interfacial processes.

To describe the capacitive response, we adopt the modeling framework inspired by the Bernards model[21], wherein modulation of channel conductivity is governed by ionic charge injected from the electrolyte into the organic semiconductor. This charge alters the doping state of PEDOT:PSS and contributes both steady-state and transient components of gate current. As illustrated in figure 9 a, the equivalent circuit of the OECT includes a channel capacitor (C_{ch})in series with a variable channel resistor $(R_{\mathrm{ch}})$and gate capacitance (C_g), capturing the key ionic–electronic transport processes[6]. The voltage drop across C_{ch} directly determines the extent of channel de-doping, making it the dominant factor linking electrochemical potential to drain current modulation[30, 35].

The fractional potential drop across the channel capacitor, U_{ch}, is expressed as[36]:

$$U_{\mathrm{ch}}(\omega) = \frac{\frac{1}{j\omega C_{\mathrm{ch}}}}{\frac{1}{j\omega C_g}+\frac{1}{j\omega C_{\mathrm{ch}}}+R_S} \tag{9}$$

As shown in figure 9b, this voltage division is strongly frequency-dependent. At low

frequencies, ionic motion is fast enough to track the gate signal, causing most of the applied potential to drop across C_{ch}, resulting in substantial de-doping and strong drain current modulation. At high frequencies, however, the capacitive reactance becomes negligible and the applied voltage drops primarily across the series resistance R_s, suppressing modulation of the channel and limiting the OECT's ability to follow rapid gate perturbations.

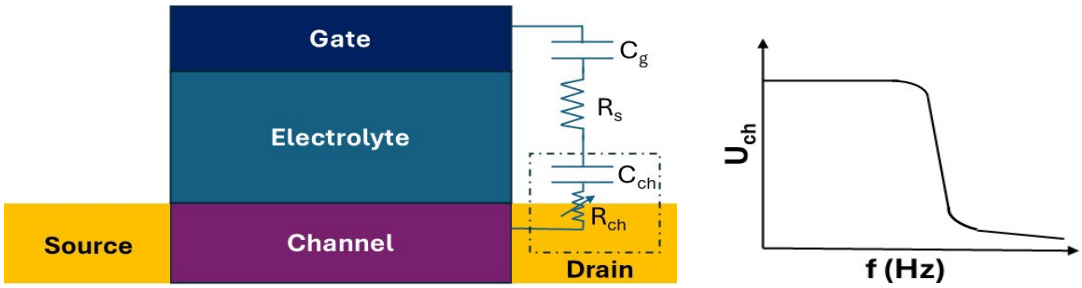

(a) (b)

Figure 9 (a) Cross-sectional schematic and equivalent circuit of the OECT, including channel capacitance (C_{ch}), gate capacitance (C_g), and series resistance (R_s); **(b)** Frequency-dependent potential drop across C_{ch} showing reduction at high frequencies.

This trend is consistent with electrochemical impedance spectroscopy (EIS) results reported by Ohayon *et. al.*[37], where effective capacitance can be derived as:

$$C = \frac{1}{2\pi f \times |Z^{img}|} \qquad (10)$$

At low frequencies, the extracted capacitance is dominated by electrical double-layer charging at the gate–electrolyte interface; at higher frequencies, the response transitions toward intrinsic gate/channel capacitance. Because ionic drift and interfacial polarization cannot follow high-frequency stimuli, C–V measurements in this regime reveal geometric and volumetric capacitance rather than parasitic effects.

To experimentally probe this intrinsic regime, high-frequency C–V measurements were performed at 10 MHz for OECTs with channel lengths of 2 mm and 4 mm, as shown in figure 10. At this frequency, double-layer formation and ionic migration are effectively suppressed, allowing the measured capacitance to reflect the volumetric dielectric properties of the PEDOT:PSS channel. The 2 mm devices exhibited higher extracted capacitance than the 4 mm devices, which we attribute to stronger electrochemical coupling and a larger effective gating area per unit length. These results highlight that channel geometry directly influences volumetric capacitance, an important consideration for high-speed sensing applications requiring rapid ionic-to-electronic transduction.

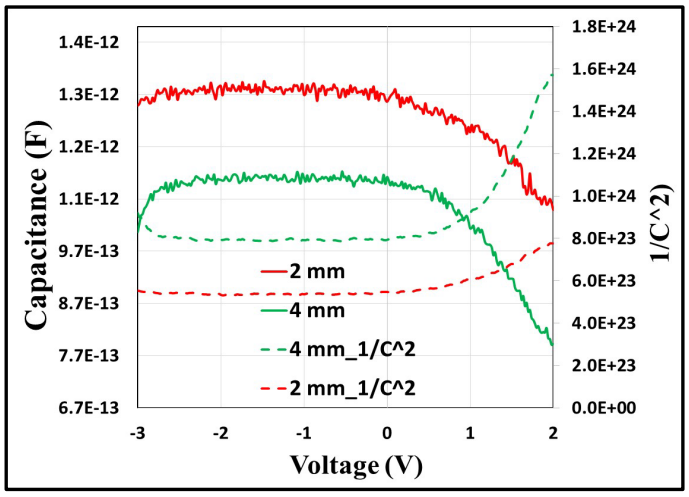

Figure 10. Capacitance–voltage (C–V) curves measured at 10 MHz for OECTs with 2 mm and 4 mm channel lengths.

To provide a concise comparison of the electrical and electrochemical behavior of devices with different channel geometries, Table 1 summarizes the key performance metrics extracted from the 2 mm and 4 mm OECTs. The table integrates the main findings across different measurement modalities—drain current, transconductance, gate leakage, capacitance, and noise performance—thereby highlighting the trade-offs associated with geometric scaling.

Table 1. Summary of key electrical parameters for 2 mm and 4 mm OECTs

Parameter	2 mm Channel OECT	4 mm Channel OECT
Maximum Drain Current (I_D,max)	Higher (~1300 µA)	Lower (~490 µA)
Maximum Transconductance (g_m,max)	Lower (~0.15 mS)	Higher (~0.45 mS)
Gate Leakage Current (I_G at −1.5V)	Low (~1.5×10^{-6} A)	Higher (~3.5×10^{-5} A)
Volumetric Capacitance (C*)	Higher	Lower
SNR Estimate (for biosensing)	~32	~18

Conclusion

In this work, we systematically investigated the electrical, electrochemical, and capacitive behavior of printed PEDOT:PSS OECTs with different channel geometries to uncover the scaling effects that govern mixed ionic–electronic transport. By correlating output and transfer characteristics with gate leakage, transconductance, and high-frequency C–V behavior, we established clear relationships between device geometry and performance. Short-channel

OECTs exhibited higher drain current, reduced gate leakage, and enhanced volumetric capacitance, enabling efficient ionic–electronic transduction and improved signal-to-noise ratio—features desirable for fast and power-constrained sensing platforms. Conversely, longer-channel devices demonstrated smoother current saturation and higher peak transconductance, but at the cost of increased leakage and noise, highlighting a fundamental trade-off between electrochemical efficiency and modulation uniformity.

Gate-current modeling and MATLAB simulations further revealed that $I_G$is an intrinsic and non-negligible component of OECT operation, particularly for non-polarizable gate materials. These results underscore the necessity of incorporating electrochemical currents and interfacial capacitance into compact models, rather than applying MOSFET-like assumptions that neglect ionic contributions. High-frequency C–V analysis confirmed that intrinsic channel capacitance dominates under rapid gating conditions, providing a pathway for decoupling parasitic double-layer effects from true volumetric response.

Overall, the combined experimental and modeling results presented here offer a deeper understanding of geometric scaling and interfacial dynamics in OECTs. These insights provide practical guidelines for optimizing future OECT designs—whether for high-speed biosensing, low-power wearable systems, or stable amplification circuits—and pave the way toward predictive models that more accurately capture the mixed ionic–electronic nature of organic electrochemical transistors.

Appendix [Optional]

Follows the Acknowledgment section. Appendices are not required to have a title or subhead. If there is only one Appendix, please label it as "Appendix". If there is more than one Appendix, they are identified as Appendix A, Appendix B, etc. Tables, figures, and equations in an appendix are labeled with "A" for a single appendix, adding a consecutive letter for each additional appendix, i.e., Eq. A-1, Eq. B-3, Table A-II, Table B-IV, Figure A-3, Figure B-5. Reference citations in an Appendix follow in consecutive order from the main text.

References

[1] H. S. White, G. P. Kittlesen, and M. S. Wrighton, "Chemical derivatization of an array of three gold microelectrodes with polypyrrole: Fabrication of a molecule-based transistor," *J. Am. Chem. Soc.*, vol. 106, pp. 5375–5377, Sep. 1984.

[2] H. F. de Paula Barbosa, A. Asyuda, M. Skowrons, A. Schander, and B. Lüssem, "Processing of organic electrochemical transistors," *MRS Commun.*, vol. 14, pp. 132–148, Feb. 2024.

[3] P. Romele, M. Ghittorelli, Z. M. Kovács-Vajna, and F. Torricelli, "Ion buffering and interface charge enable high-performance electronics with organic electrochemical transistors," *Nat. Commun.*, vol. 10, Jul. 2019, Art. no. 3044.

[4] J. T. Friedlein, R. R. McLeod, and J. Rivnay, "Device physics of organic electrochemical transistors," *Org. Electron.*, vol. 63, pp. 398–414, Dec. 2018.

[5] D. Khodagholy *et al.*, "High-transconductance organic electrochemical transistors," *Nat. Commun.*, vol. 4, Jul. 2013, Art. no. 2133.

[6] J. Rivnay *et al.*, "Organic electrochemical transistors," *Nat. Rev. Mater.*, vol. 3, Dec. 2018, Art. no. 17086.
[7] Y. Fang, X. Li, and Y. Fang, "Organic bioelectronics for neural interfaces," *J. Mater. Chem. C*, vol. 3, pp. 6424–6430, Jun. 2015.
[8] M. Berggren and A. Richter-Dahlfors, "Organic bioelectronics," *Adv. Mater.*, vol. 19, no. 20, pp. 3201–3213, Oct. 2007.
[9] K. Feron *et al.*, "Organic bioelectronics: Materials and biocompatibility," *Int. J. Mol. Sci.*, vol. 19, Aug. 2018, Art. no. 2382.
[10] J. Rivnay *et al.*, "High-performance transistors for bioelectronics through tuning of channel thickness," *Sci. Adv.*, vol. 1, May. 2015, Art. no. e1400251.
[11] D. Khodagholy *et al.*, "High-transconductance organic electrochemical transistors," *Nat. Commun.*, vol. 4, Jul. 2013, Art. no. 2133.
[12] S.-M. Kim *et al.*, "Influence of PEDOT:PSS crystallinity and composition on electrochemical transistor performance and long-term stability," *Nat. Commun.*, vol. 9, Sep. 2018, Art. no. 3858.
[13] A. F. Paterson *et al.*, "Water stable molecular n-doping produces organic electrochemical transistors with high transconductance and record stability," *Nat. Commun.*, vol. 11, Jun. 2020, Art. no. 3004.
[14] Y. Yao *et al.*, "Flexible and stretchable organic electrochemical transistors for physiological sensing devices," *Adv. Mater.*, vol. 35, Feb. 2023, Art. no. 2209906.
[15] J. Ajayan *et al.*, "Organic electrochemical transistors (OECTs): Advancements and exciting prospects for future biosensing applications," *IEEE Trans. Electron Devices*, vol. 70, no. 7, pp. 3401–3412, Jul. 2023.
[16] H. Liu, J. Song, Z. Zhao, S. Zhao, Z. Tian, and F. Yan, "Organic electrochemical transistors for biomarker detections," *Adv. Sci.*, vol. 11, Jan. 2024, Art. no. 2305347.
[17] Q. Song *et al.*, "Fabrication of PEDOT:PSS-based solution-gated organic electrochemical transistor array for cancer-cell detection," *RSC Adv.*, vol. 13, pp. 36416–36423, Dec. 2023.
[18] R. B. Rashid, X. D. Ji, and J. Rivnay, "Organic electrochemical transistors in bioelectronic circuits," *Biosens. Bioelectron.*, vol. 190, Oct. 2021, Art. no. 113461.
[19] J. Ajayan, P. Mohankumar, R. Mathew, L. R. Thoutam, B. K. Kaushik, and D. Nirmal, "Organic electrochemical transistors (OECTs): Advancements and exciting prospects for future biosensing applications," *IEEE Trans. Electron Devices*, vol. 70, no. 7, pp. 3401–3412, Jul. 2023.
[20] X. Strakosas, M. Bongo, and R. M. Owens, "The organic electrochemical transistor for biological applications," *J. Appl. Polym. Sci.*, vol. 132, Apr. 2015, Art. no. 41735.
[21] D. A. Bernards and G. G. Malliaras, "Steady-state and transient behavior of organic electrochemical transistors," *Adv. Funct. Mater.*, vol. 17, pp. 3538–3544, Oct. 2007.
[22] J. Rivnay *et al.*, "Structural control of mixed ionic and electronic transport in conducting polymers," *Nat. Commun.*, vol. 7, Apr. 2016, Art. no. 11287.
[23] R. Giridharagopal *et al.*, "Electrochemical strain microscopy probes morphology-induced variations in ion uptake and performance in organic electrochemical transistors," *Nat. Mater.*, vol. 16, pp. 737–742, Jun. 2017.
[24] S. Inal, G. G. Malliaras, and J. Rivnay, "Benchmarking organic mixed conductors for transistors," *Nat. Commun.*, vol. 8, Nov. 2017, Art. no. 1767.

[25] S. Z. Riam, M.N.Islam, T. Sarker, V. Budhraja and S. Tabassum, “Flexible Organic Electrochemical Transistor Based on Conjugated Conducting Polymers” *ECS Trans.*, vol. 113, no. 6, pp. 7-17, May 2024.
[26] A. Markova, S. Střitěnský, M. Weiter, and M. Vala, “Serial resistance effect on organic electrochemical transistors’ transconductance,” *IEEE Sens. J.*, vol. 23, no. 17, pp. 19417–19423, Sep. 2023.
[27] J. T. Friedlein, R. R. McLeod, and J. Rivnay, “Device physics of organic electrochemical transistors,” *Org. Electron.*, vol. 63, pp. 398–414, Dec. 2018.
[28] D. A. Bernards, D. J. Macaya, M. Nikolou, J. A. DeFranco, S. Takamatasu and G. G. Malliaras, Enzymatic Sensing with Organic Electrochemical Transistors,” *J. Mater. Chem.*, vol. 18, pp. 116-120, Oct. 2007.
[29] V. Athanasiou, S. Pecqueur, D. Vuillaume, and Z. Konkoli, “On a generic theory of the organic electrochemical transistor dynamics,” *Org. Electron.*, vol. 72, pp. 39–49, Sep. 2019.
[30] V. Kaphle, P. R. Paudel, D. Dahal, R. K. R. Krishnan, and B. Lüssem, “Finding the equilibrium of organic electrochemical transistors,” *Nat. Commun.*, vol. 11, May 2020, Art. no. 2515.
[31] M. Zabihipour *et al.*, “High-yield manufacturing of fully screen-printed organic electrochemical transistors,” *NPJ Flex. Electron.*, vol. 4, Aug. 2020, Art. no. 15.
[32] M. Skowronski, D. Dahal, P. R. Paudel, and B. Lüssem, “Depletion-type organic electrochemical transistors and the gradual-channel approximation,” *Adv. Funct. Mater.*, vol. 34, Jan. 2024, Art. no. 2303324.
[33] A. Shirinskaya *et al.*, “Numerical modeling of an organic electrochemical transistor,” *Biosensors*, vol. 8, no. 4, Oct. 2018, Art. no. 103.
[34] G. C. Faria, D. T. Duong, and A. Salleo, “On the transient response of organic electrochemical transistors,” *Org. Electron.*, vol. 45, pp. 215–221, Jun. 2017.
[35] G. C. Faria, D. T. Duong, A. Salleo, C. Polyzoidis, S. Logothetidis, J. Rivnay, R. Owens, G. G. Malliaras, *MRS Commun,* vol. 4, no. 4, pp. 189-194, Dec 2014.
[36] J. Nissa, P. Janson, M. Berggren, and D. T. Simon, “The role of relative capacitances in impedance sensing with organic electrochemical transistors,” *Adv. Electron. Mater.*, vol. 7, Apr. 2021 Art. no. 2001173.
[37] D. Ohayon, V. Druet, and S. Inal, “A guide for the characterization of organic electrochemical transistors and channel materials,” *Chem. Soc. Rev.*, vol. 52, pp. 1001–1023, Jan. 2023.